Hydrogen adsorption of nickel-silica materials: Role of the SBA-15 porosity

P.M. Carraro [a, b, *], A.A. García Blanco [d], C. Chanquía [c], K. Sapag [d], M.I. Oliva [a], G.A. Eimer [b]

[a] Instituto de Física Enrique Gaviola (IFEG/UNC-CONICET), Córdoba, Argentina
[b] Centro de Investigación y Tecnología Química (CITeQ/UTN-CONICET), Córdoba, Argentina
[c] Centro Atómico Bariloche, Comisión Nacional de Energía Atómica (CAB-CNEA), San Carlos de Bariloche, Río Negro, Argentina
[d] Laboratorio de Sólidos Porosos (INFAP/ UNSL-CONICET), San Luis, Argentina

ARTICLE INFO

ABSTRACT

In this work, SBA-15 support was impregnated with nickel in order to study the influence of different factors (metal content, support, method of preparation) on their hydrogen storage capacity. H$_2$ adsorption was measured at low and high pressures (up to 10 and 40 bar) at 77 and 293 K, evaluating the influence of metallic nickel on such adsorption capacity. The properties of the prepared materials were studied by N$_2$ adsorption-desorption, XRD, TPR, UV−Vis, TEM, SEM and XPS techniques. The results indicated the importance of the nickel dispersion on the support to improve hydrogen storage. Thus, Ni/SBA-15 (2.5) sample, in contrast to Ni/SBA-15 (2.5)-R, shows the higher hydrogen adsorption capacity at both 77 K and 293 K.

© 2017 Published by Elsevier Inc.

1. Introduction

One of the most important challenges for the so-called "hydrogen economy" is hydrogen storage. Hydrogen is an energy carrier which holds tremendous promise as a new renewable, versatile and clean energy alternative. The gravimetric energy density of hydrogen is nearly three times greater than that of other chemical fuel. However, the volumetric energy density of hydrogen is very low compared to gasoline or natural gas [1], thus, from the application point of view it is not a practical option for on-board vehicles. A key technical challenge is to find the most effective way to store hydrogen in order to replace the current fuel systems.

During the last years there have been many studies to develop nanoporous materials as hydrogen storage systems that meet the targets proposed by the US Department of Energy (DOE) and the European Hydrogen & Fuel Cell Technology Platform. Among the materials that could be used, high-surface adsorbents are an alternative, and among them carbon nanotubes, nanofibers, polymer nanocomposites, metal organic frameworks, zeolites and other nanostructured and porous materials have been the subject of research [2−4]. Porous solids offer an interesting opportunity for hydrogen storage under safe and reversible conditions.

The main properties of nanoporous materials, which can be modified in order to improve hydrogen adsorption, are the adsorbent-adsorbate interaction, specific surface area, geometry and pore size. In addition, the incorporation of metals in nanoporous materials has shown to improve H$_2$ adsorption, both at 77 K and room temperature [5,6]. This behavior could be related with the affinity of metals towards H$_2$, suggesting that highly dispersed metal clusters or nanoparticles on nanoporous supports can enhance hydrogen uptakes [7].

Ordered mesoporous silicas, such as SBA-15, are considered as suitable adsorbents due to its high surface area, pore volume, ordered pore structure and high capacity to functionalize its surface. Several strategies and methods have been designed to prepare supported metal oxide catalysts with different metal loading and high dispersion. Thus, the coalescence of metal particles during the synthesis should be avoided in order to obtain support material with well-dispersed metal centers.

Bouazizi et al. [8] have found that high dispersion of fine metal particles promotes affinity towards molecular hydrogen. Meanwhile, Lee et al. [9] have reported that the amount of hydrogen adsorbed increased after Pd-doping, without destroying the mesoporous structure. Han et al. [10] studied the influence of different

Ti doping levels on the hydrogen adsorption characteristics of SBA-15 materials prepared by direct one-step synthesis. Their results suggested that hydrogen adsorption was not only affected by the titanol and bridging hydroxyl groups generated, but also by the increased number of micropores. In addition, Acatrinei et al. [11] reported, using Inelastic Neutron Scattering, that hydrogen adsorption over Ti-SBA-15 occurred on titanol groups, generated around Ti, and in bridging hydroxyls. Prasanth et al. [12] have reported that nickel loading on the mesoporous silica framework (SBA-15, MCM-41, MCM-48) decreases hydrogen adsorption at 77 K (up to 112 kPa) regarding the pure support. However, the hydrogen storage capacity for nickel-loaded materials, increased at 303 K (up to 4000 kPa).

The motivation of the present study was to evaluate the effect of the porous characteristics of the SiO_2 material, over the hydrogen adsorption capacity of mesoporous materials modified with nickel. In this regard, we used a SBA-15 material as a support, in order to compare the effect of changing the pore size and connectivity, with respect to our previous findings with the Ni/MCM-41 samples [13,14]. As a way of comparison, we used the same different Ni loading (2.5 and 10 wt.%) by a wet impregnation method, and measured hydrogen adsorption at 77 and 293 K, at pressures of up to 10 and 40 bar, respectively. In addition, the samples were reduced by a H_2 flow in order to study the influence of metallic nickel on the hydrogen adsorption. The materials were also characterized using transmission electron microscopy (TEM), N_2 adsorption-desorption, X-ray diffraction (XRD), scanning electron microscopy (SEM), temperature-programmed reduction (TPR), UV—Vis diffuse reflectance spectroscopy and Inductively Coupled Plasma Atomic Emission Spectroscopy (ICP), in order to investigate the effects of the textural and chemical properties of Ni/SBA-15 material on hydrogen-storage behavior.

2. Material and methods

2.1. Synthesis

The pure SBA-15 was synthesized dissolving 4.0 g of Pluronic P123 (poly ethylene glycol block, Aldrich) in 30 g of water and 120 g of 2 M hydrochloric acid aqueous solution (HCl) under stirring at 313 K. Then 8.50 g of tetraethoxysilane (TEOS, Aldrich 98%) was added into this solution with stirring at 313 K for 20 h. The mixture was aged at 373 K overnight without stirring. The solid product was filtered, washed, and air-dried at 333 K overnight. Calcination was carried out in air by a rate of 1 K/min to 773 K for 9 h. Then, SBA-15 silica was modified by the incipient wet impregnation method. Aqueous solutions of nickel ($Ni(NO_3)_2.6H_2O$, Merck) with different concentrations were used to reach theoretical metal loadings (2.5 and 10 wt.%). The SBA-15 host (0.75 g) was added in the precursor solution at room temperature and the water was removed slowly by rotary evaporation at 323 K for about 30 min. The resulting powder was dried at 333 K and calcined for 9 h at 773 K. The samples were labeled as Ni/SBA-15(x) where "x" is the theoretical metal loading in wt.%.

For the reduction of nickel oxide to metallic nickel, the samples were treated under H_2 flow for 5 h with a heating rate of 1 K/min at 723 K. The resulting materials were denoted as Ni/SBA-15 (2.5)-R and Ni/SBA-15 (10)-R.

2.2. Characterization

The textural characterization was carried out by N_2 adsorption-desorption isotherms at 77 K conducted in a Micromeritics ASAP 2000. The samples were previously vacuum-degassed at 523 K for 6 h. The specific surface area (S_{BET}) for each catalyst was calculated

using adsorption data by the Brunauer-Emmett-Teller method in the pressure range of p/p^0: 0.01—0.25. The pore volume and pore size distributions (PSD) were determined by the Nonlocal Density Functional Theory (NLDFT) method. This adjustment was made using the ASiQwin software from Quantachrome Instruments. Mesopore size distribution was calculated from N_2 adsorption-desorption isotherm using desorption branch and the kernel "N_2 at 77 K on silica, cylindrical pore, equilibrium" of the mentioned software. The microporosity was examined by application of the α-plot method to the adsorption data for N_2, using the reference isotherm for non-porous silica LiChrospher Si-1000 [15].

The structural characterization of the materials was performed by X-ray diffraction (XRD) in PANanalytical Empyrean diffractometer with Cu Kα radiation (λ = 1.5418 Å) in the range of *2θ* from 0.7 to 7° and from 10 to 80°. The interplanar distance (d_{100}) was estimated using the position of the first X-ray diffraction line. The lattice parameter (a_0) of the hexagonal unit cell was calculated as $a_0 = (2/\sqrt{3}) d_{100}$. The interplanar spacing (d_{100}) and the estimated V_{MP} (volume of primary mesopores) are used to calculate the diameter of the primary mesopores (w_p), following the procedure described by Kruk et al. [16], applicable to materials with infinite array of cylindrical pores arranged in a hexagonal pattern. The w_p is obtained by the following equation:

$$w_p = c \cdot d_{100} \cdot \left(\frac{v_{mp}}{\frac{1}{\rho} + v_{mp} + v_{\mu p}} \right)^{1/2} \tag{1}$$

where c is a constant associated with a hexagonal packed array with uniform cylindrical pores, the d_{100} is the planar space obtained by XRD pattern and ρ is the density of the pore walls considered to be equal to the density of the amorphous silica (2.2 g/cm^3).

Transmission electron microscopy (TEM) images were obtained using a Philips CM200UT transmission electron microscope. Samples were dispersed in ethyl alcohol 99.5% and a drop of the suspension was deposited on a lacey carbon copper grid.

The scanning electron microscopy (SEM) images of the materials were obtained in a SEM-FEG Nova NANO-SEM 230. Gold coverage was applied to make samples conductive. The acceleration voltage was 20 kV.

The Ni content was determined by Inductively Coupled Plasma Atomic Emission Spectroscopy (ICP-OES) using a spectrophotometer Thermo Scientific 7400 combined with microwave digestion.

UV—Vis diffuse reflectance spectra (UV—Vis DRS) were performed on Jasco 650 spectrometer with an integrating sphere in the wavelength range of 200—900 nm. The data were automatically transferred according to the Kubelka-Munk equation:

$$f(R) = (1 - R_\infty)^2 / 2R_\infty \tag{2}$$

The reducibility of the calcined nickel catalyst was studied by H_2 Temperature-Programmed Reduction (TPR) in the Micromeritic ChemiSorb 2720 Instrument. In these experiments, the samples were heated from 298 to 1073 K at a rate of 10 K/min in the presence of 5% H_2/N_2 gas mixture (20 mL/min STP), and the reduction reaction was monitored by the H_2 consumption with a built-in thermal conductivity detector (TCD).

X-ray photoelectron spectra (XPS) were obtained in a VG Microtech ESCA apparatus equipped with an Al anode (Al Ka radiation, 1486.6 eV) and VG100AX spherical analyzer. The binding energy was referred to the Si 2p line at 103.4 eV.

Hydrogen (99.999%) adsorption measurements were carried out at 77 K and pressures up to 10 bar in an automatic manometric system ASAP 2050 (Micromeritics Instrument Corporation).

Approximately 200−300 mg of sample was used for each measurement.

High-pressure adsorption isotherms of hydrogen (99.999%) were measured at 293 K using a high-pressure manometric system HPA 100 (VTI Corporation). Previous to all the adsorption experiments, the samples were degassed under vacuum conditions (5.10^{-3} mmHg) at 573 K during 5 h to completely remove any residual water in order to obtain the highest gas adsorption capacity. Leak testing of pressure equipments is performed with helium, prior to the performance of measurements using hydrogen. Helium was used to measure the void volume of the sample cell in both instruments, before each analysis.

3. Results and discussion

3.1. N₂ adsorption-desorption

Nitrogen adsorption-desorption is one of the most employed methods of characterization of porous materials. Fig. 1 shows the N₂ adsorption-desorption isotherms of the samples, and the textural parameters calculated from the adsorption isotherms are collected in Table 1. The isotherms shapes are characteristic of ordered porous materials, with well-defined H1-type hysteresis loops, according to the IUPAC classification [17,18]. This type of hysteresis loops is associated with capillary condensation and desorption in open-ended cylindrical mesopores, which is typical of materials with cylindrical geometries and uniform pore size [19]. The materials also adsorb N₂ at very low pressures ($p/p^0 < 0.05$), a fact related to micropore filling or strong adsorbate-adsorbent interactions.

On the other hand, changes in the Ni/SBA-15 isotherms are observed with respect to the unloaded SBA-15 used as support material. It is noteworthy the change of shape in the hysteresis loop for the nickel-loaded materials [20]. The hysteresis loop of the Ni-

loaded samples extends to relative pressures close to 0.47, indicating changes in the porous geometry in those materials compared to the original SBA-15. This behavior has been previously assigned to the presence of particles inside the mesopores of SBA-15, and is an evidence of the presence of nickel oxide nanoparticles inside the mesopores of the parent SBA-15 [21−23].

In the pore size distribution plot (PSD, Fig. 2), it is observed that the samples show a defined pore size in the mesoporous range, between 6 and 8 nm; in addition, it is evident the presence of micropores. Additionally, the cumulative pore volume is represented in Fig. 2, showing the pore volume correspondence with the sample pore size. Table 1 summarizes the micropore volume $V_{\mu p}$ and primary mesoporous volume V_{MP}, which were calculated using the α-plot method. These values could be compared with the cumulative pore volume values. The samples presented some microporosity, which was also inferred from PSD (Fig. 2). The average size of the mesopores, the micropore volume and the S_{BET} specific area decreased with increasing Ni loading, in accordance with the discussion above. As was mentioned previously, this fact is due to the presence of large particles on the external surface as well as nanoparticles and/or clusters of oxides inside the pore channels.

3.2. X-ray diffraction

Fig. 3 a shows the low-angle XRD patterns of pure SBA-15 and Ni/SBA-15 samples. It can be seen that all the samples exhibited XRD patterns with one very intense diffraction peak indexed to the (100) plane, and two weak intense peaks indexed to the (110) and (200) planes, which are characteristic of 2-D hexagonal (P6mm) structure with highly ordered structure [24,25]. The low angle XRD patterns of the nickel loaded samples are similar to that of the unloaded SBA-15, indicating that the structure was preserved regardless of the nickel loading, in good agreement with the obtained results by N₂ adsorption-desorption isotherms. However, a decrease in the intensity of the main peak was observed, suggesting some loss in the periodicity of the SBA-15 pore structure.

On the other hand, the primary mesopores diameter (w_p) was calculated from the d_{100} and the V_{MP} values using equation (1). The results for all samples are similar to that obtained in the PSD by NLDFT method.

The high-angle XRD patterns of the Ni/SBA-15 samples are shown in Fig. 3 b. All of the patterns exhibited similar diffraction peak positions, indicating that similar phases were dispersed on the surface support. Both samples presented three narrow and intense peaks at $2\theta = 37°$, $43°$ and $64°$. In addition, the Ni/SBA-15 (10) sample also exhibited diffraction peaks at $75.5°$ and $80°$. All of these peaks are assigned to different crystal planes of NiO phase [26,27]. It was also found that the intensity of the XRD peaks increase with the increase of the nickel content, indicating the increase of the amount of NiO particles.

Fig. 4 shows the high-angle XRD patterns of the samples after the H₂ reduction process. The Ni/SBA-15 (10) sample presents three peaks at $2\theta = 44.6$, 51.8 and $76.5°$, indicating the presence of metallic nickel. In the case of Ni/SBA-15 (2.5) sample only appears a peak at $44.6°$. In addition, it is shown the peaks attributable to nickel oxide disappeared. These results suggest that NiO in the samples was reduced to Ni⁰.

3.3. Morphological studies

The mesostructure of the materials was also investigated with TEM. Fig. 5 a-b-c shows straight mesochannels arraying along the long axis, characteristics of the SBA-15 materials [28,29]. Also, the hexagonal arrangement of the unidirectional mesopores is observed in Fig. 5 b-c-e. It is important to note, that even after the
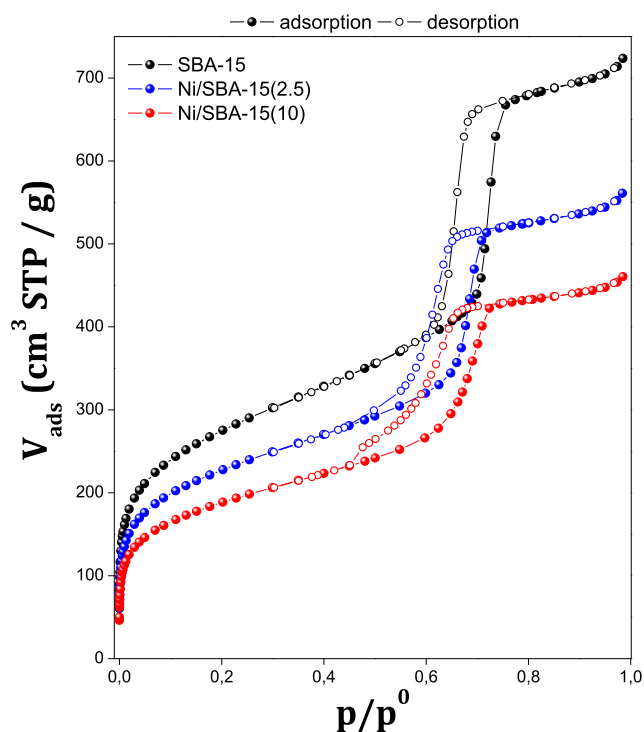

Fig. 1. N₂ adsorption-desorption isotherms at 77 K of the SBA-15 and Ni/SBA-15 materials.

Table 1
Textural properties and chemical composition of the synthesized materials.

Sample	Area $(m^2/g)^a$	Ni content $(wt.\%)^b$	D_p $(nm)^c$	$V_{\mu p}$ $(cm^3/g)^d$	V_{MP} $(cm^3/g)^d$	V_{TP} $(cm^3/g)^c$
SBA-15	992	–	7.4	0.06	0.80	1.20
Ni/SBA-15 (2.5)	819	2.13	6.8	0.07	0.67	0.87
Ni/SBA-15 (10)	678	12.9	6.9	0.05	0.52	0.71

[a] Determined by BET.
[b] Determined by ICP.
[c] Pore diameter (D_P) and Pore volume (V_{TP}) determined by DTP.
[d] Volume of primary mesopores (V_{MP}) Determined by α-plot method.
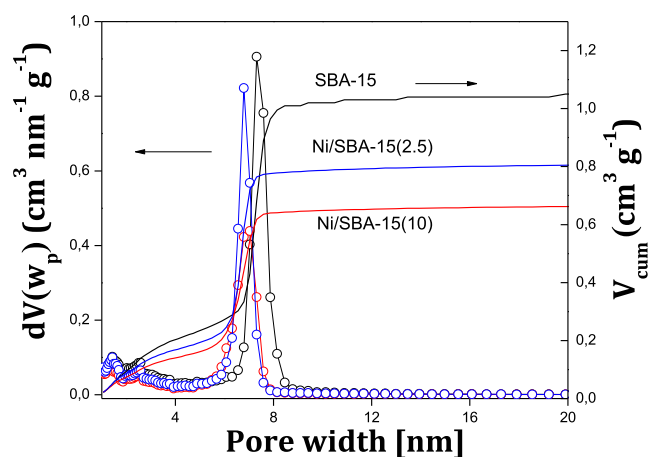
Fig. 2. NLDFT pore size distribution and cumulative pore volume distributions of the SBA-15 and Ni/SBA-15 materials.

Ni loading, the mesoporous structure of SBA-15 support has been well preserved. The average pore diameter of samples was about 7 nm. These results were in accordance with the results of low-angle XRD and N_2 adsorption-desorption study.

In Fig. 5 d-e-f₁ it can be observed irregularly distributed high-contrast areas, which evidenced the presence of segregated nickel oxide species on the external surface of the support. These oxides have an average diameter of 10–30 nm and 30–80 nm for the Ni/SBA-15 (2.5) and Ni/SBA-15 (10) samples, respectively. This feature was mainly observed for the sample with high Ni loading and is in good agreement with the data reported [30,31], where a migration of the Ni oxides to the outside of the support during the calcination procedure was observed. These Ni oxide particles cause partial blocking pores, which is in agreement with N_2 adsorption results. In order to distinguish the oxides nanoparticles in the support, dark-field images (Fig. 5 f₂) were obtained, where Ni oxide species were evidenced by the brighter contrast.

In previous reports [13,14], we could observe that the smaller pore size of the MCM-41 allows to stabilize small oxide nano-clusters or nanoparticles on the surface as well as inside the mesochannels. This fact would be evidencing the refiner effect carried out by the support structure, whose pore diameter limits the size of the metal nanospecies formed inside them. Therefore, the results indicated that the larger particle size of nickel oxide was controlled by pore size of the SBA-15 support.

On the other hand, it was possible to corroborate the structural regularity of the samples after the reduction treatment. The TEM images of the reduced samples are shown in Fig. 6, and they show the preservation of the host structure as well.

The typical morphology of SBA-15 and a representative image of Ni/SBA-15 are illustrated in Fig. 7. These images show some short rods with uniform size which appear to be aggregated into wheat-like morphology [32,33]. As it can be seen from Fig. 7a and b, the

morphology of SBA-15 was maintained, after the nickel loading. In order to determine the presence of nickel in the Ni/SBA-15, EDS analysis (Fig. 7c and d) was carried out, which indicates the elemental compositions of O, Si and Ni.

3.4. UV–Vis DRS spectroscopy

Diffuse reflectance UV–Vis spectra were recorded for NiO reference sample and calcined Ni/SBA-15 samples in order to study the coordination environment of Ni. The samples spectra are shown in Fig. 8, which contain an intense absorption in the UV region, in the 250–350 nm range, with two maxima at 260 nm and about 296–300 nm. This last band can be assigned to the $O^{2-}(2p) \rightarrow Ni^{2+}(3d)$ charge transfer transition of octahedral Ni^{2+} species in NiO lattices [34]. This absorption increases in intensity and its position slightly shifted toward higher wavenumber for the Ni/SBA-15 (10) sample. It is well known that the position of the absorption edge of semiconductor powders is strongly affected by particle size, shifting significantly to lower wavelength by decreasing particle size. Accordingly, depending on shape and size of the NiO particles, the absorption in the UV region is reported to change in shape and position [35]. Thus, the size of the NiO particles in the samples is different and probably of diverse interaction with the support, which is in agreement with the XRD and the TPR results. In addition, another absorption band edge appears at around 260 nm, for both samples, which could be associated with the presence of isolated mononuclear Ni^{2+} species interacting with the mesoporous framework oxygen, related to a $O^{2-} \rightarrow Ni^{2+}$ charge transfer transition in the mesoporous lattice.

On the other hand, the samples also show absorption bands at about 400–600 and 700–900 nm. These bands have been assigned to Ni^{2+} in octahedral coordination in NiO [35,36] and are significantly more intense for the Ni/SBA-15 (10) sample. Taking this into account, it can be concluded that the presence of clusters or nanoparticles with a local structure similar to the NiO, as well as their sizes and interactions with the mesoporous material are modified by increasing the metal loading. These results are in accordance with our previous works using MCM-41 as a support of nickel at different loading [13].

3.5. X-ray photoelectron spectra (XPS)

XPS spectra of the reduced and unreduced Ni/SBA-15 are shown in Fig. 9. The spectra show that nickel in the unreduced samples (Ni/SBA-15 (2.5) and Ni/SBA-15 (10)) is mainly in its Ni^{2+} oxidation state (NiO), since the shape of the spectra for these samples show the characteristic multi-peak feature for this compound [37]. In addition, the main peak of Ni $2p_{3/2}$ corresponds to the reported value for nickel in that oxidation state, at 854 eV [37]. In addition, the value of the spin-orbit splitting observed (18.3 eV) between the main peaks Ni $2p_{3/2}$ and $2p_{1/2}$ of corresponds to the one reported for NiO. There is a remarkable difference of intensity between the samples with different metal loading. The signal observed for the

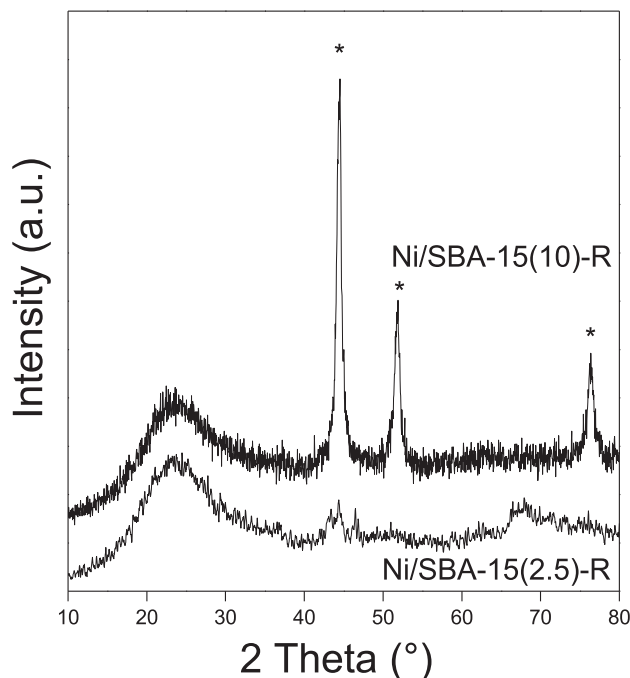**Fig. 4.** High-angle XRD patterns of Ni/SBA-15-R samples.
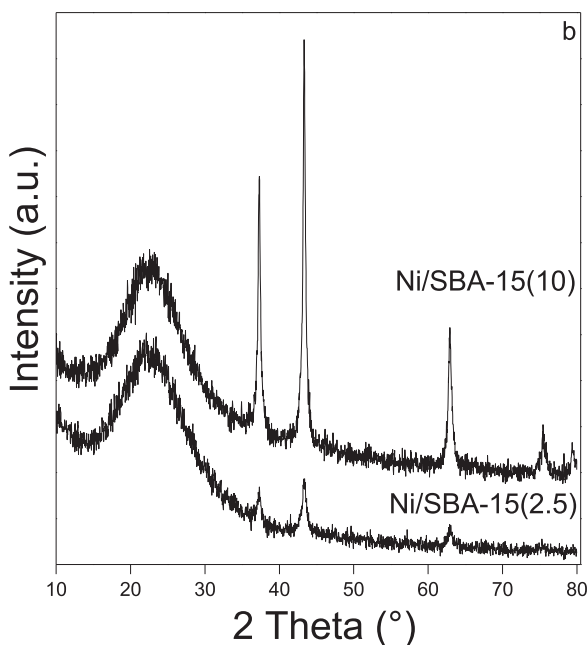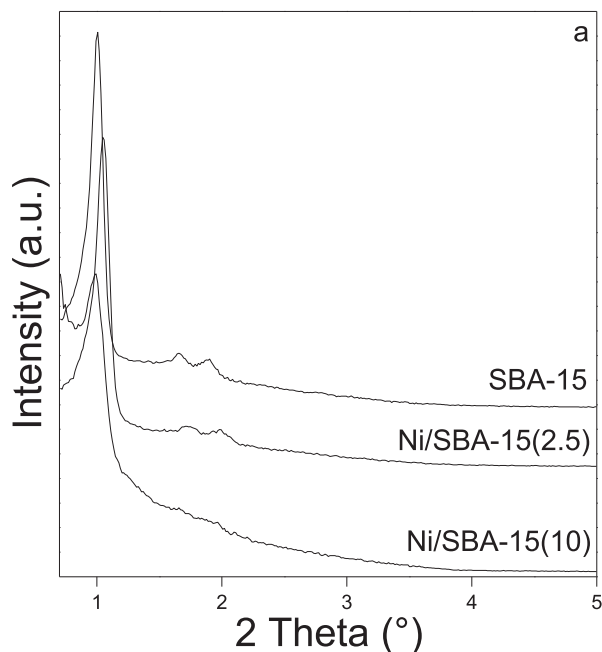
Fig. 3. Low-angle XRD patterns (a) and high-angle XRD patterns (b) of the SBA-15 and Ni/SBA-15 materials.

sample Ni/SBA-15 (2.5) presents a low intensity, a fact related with the low concentration of nickel in this sample.

In Fig. 9 are also shown the spectra of the reduced samples (Ni/SBA-15 (2.5)-R and Ni/SBA-15 (10)-R). For the sample Ni/SBA-15 (2.5)-R, a peak broadening compared to the spectrum of the un-reduced sample could be inferred, but there is not enough evidence, due to the low intensity of the peak. On the other hand, for the Ni/SBA-15 (10)-R sample, there is a clear peak broadening, and a

new contribution of a peak at 852.1 eV is observed. This value of binding energy corresponds to the Ni $2p_{3/2}$ of metallic nickel, or Ni^0 [37]. As a result, in the XPS spectrum of the Ni/SBA-15 (10)-R sample, we observed the contributions of both nickel oxide (NiO) and metallic nickel. This is an evidence of the reduction to metallic nickel of some of the nickel oxide particles of the sample after the reductive treatment performed to the samples. The NiO observed in this sample could be attributed to surface oxides formed on the sample due to contact with air.

3.6. Temperature-programmed reduction

TPR is a convenient technique to study the reduction process of metal-oxide species supported on the catalysts. The temperature reduction depends of the different factors such as the particle size, the interaction with the support and nature of the metal oxide. The TPR profiles of the Ni/SBA-15 samples are shown in Fig. 10. According to previous investigations, Ni^{2+} is reduced to Ni^0 without going through intermediate oxides, and therefore H_2 consumption peaks appearing at different temperatures should be assigned to different species. The bulk NiO has a reduction peak around 568 K [38].

For both samples, only one reduction peak could be distinguished, about at ~660 K assigned to reduction of Ni^{2+} to Ni^0 from NiO on the external surface of SBA-15 [39]. In addition, the Ni/SBA-15 (10) sample presents a shoulder about 820 K. This could be associated to the reduction of smaller NiO nanoparticles or with a stronger interaction with the support [40], which may be probably confined within the mesopores channels. Our previous TPR studies reported that Ni/MCM-41 material [14] present higher reduction temperatures than the Ni/SBA-15, which is indicative of a high dispersion of nickel species strongly interacting with the support. This high reduction temperature can be awarded to the shielding effect of the MCM-41 framework on nickel species from H_2 "attack" [41].

Thus, the nickel species on the SBA-15 support are easier to reduce and also more easily sintered, due their weak interaction
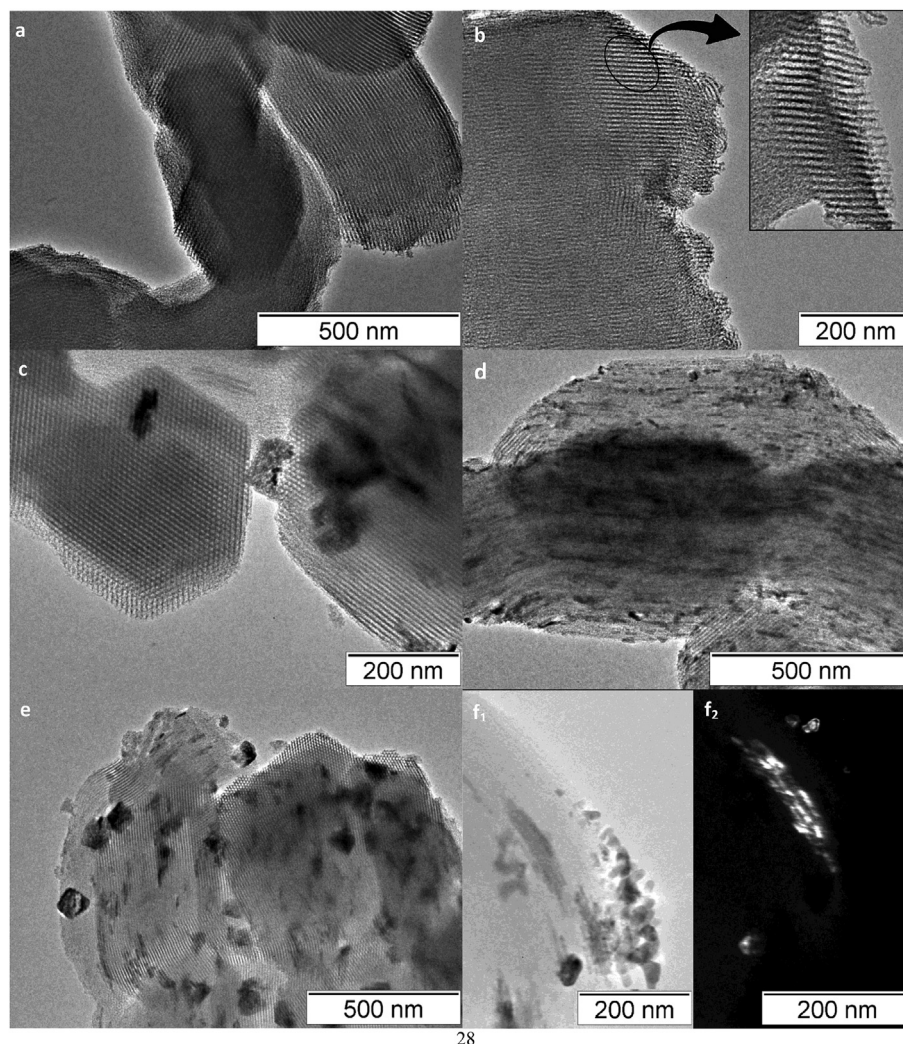
Fig. 5. Transmission electron microscopy images of (a–b) SBA-15, (c–d) Ni/SBA-15 (2.5) and (e-f₁-f₂) Ni/SBA-15 (10).

with the support, resulting in larger particles size. It is known that this type of particles and the proportion of them are important for controlling a metal well-dispersion on the support for the hydrogen adsorption.

4. Hydrogen uptake measurements

The hydrogen storage capacity at 77 K was evaluated at low and high pressures for the Ni/SBA-15 samples, both for the calcined samples and those subjected to a reduction process. Fig. 11 a shows the hydrogen excess isotherms of all the samples from 0 to 10 bar at 77 K. The hydrogen adsorption of the samples showed to be completely reversible, without hysteresis phenomena. The Ni/SBA-15 (2.5) isotherm shows that the saturation is not attained at 10 bar, which indicate that higher H_2 adsorption capacity is possible at upper pressures. This fact is in concordance with our previous results [13,14].

Fig. 11 b shows the behavior at low pressures, up to 1 bar. At lower pressures, the H_2 uptake depends mainly on the strength of the interactions between adsorbate and adsorbent [3]. It is interesting to note that, the Ni/SBA-15 (2.5) and the SBA-15 samples present similar behavior at low pressures, which suggest a low interaction between the nickel species and H_2 molecule. In concordance with our results Prasanth et al. [12] have reported that

nickel incorporation into mesoporous silica decreases the hydrogen adsorption at 77 K up to 1 bar. However, working at pressures up to 10 bar, a pronounced enhancement of H_2 adsorption capacity for the Ni/SBA-15 (2.5) sample was observed. The maximum capacity of hydrogen adsorption, of about 1.2 wt.%, was reached for this sample, meanwhile the SBA-15 sample show a minor adsorption capacity. Thus, although the SBA-15 sample presents the highest specific surface area, this minor amount adsorbed is due to the weak van der Waals interactions between SBA-15 and H_2 molecule, which indicates that the maximum hydrogen adsorption would not depend on its porosity, but of the composition or nature of the material and the metal species present on the surface.

The Ni/SBA-15 (2.5) sample presented the highest hydrogen storage capacity, probably due to the nickel species finely dispersed on the support. In our previous reports [1,2], the role of these sites responsible of the H_2 adsorption on Ni/SiO$_2$ system was evidenced by the Density Functional Theory calculations, where the enhancement of H_2 interaction was observed for Ni atoms with low coordination. Therefore, this fact helps to explain the behavior shown by the Ni/SBA-15 (2.5) sample at 77 K, where such Ni sites could interact strongly with the H_2 molecules, increasing the adsorption in comparison with the pure SBA-15 support. Moreover, it is well-known that the total volume of micropores can contribute to the enhanced hydrogen adsorption, since the narrow pores have
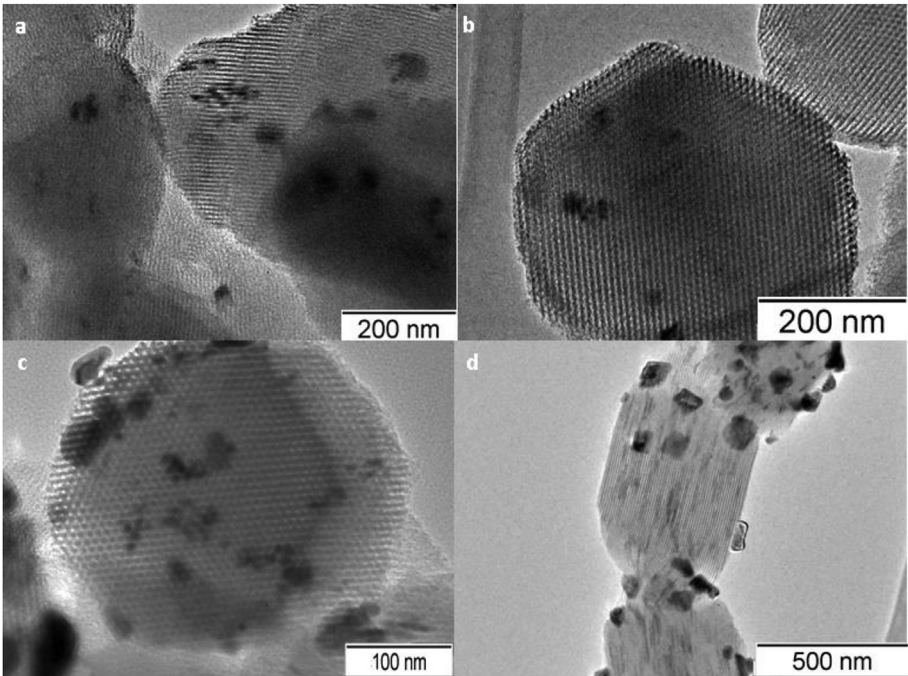
Fig. 6. Transmission electron microscopy images of (a–b) Ni/SBA-15 (2.5)-R and (c–d) Ni/SBA-15 (10)-R.
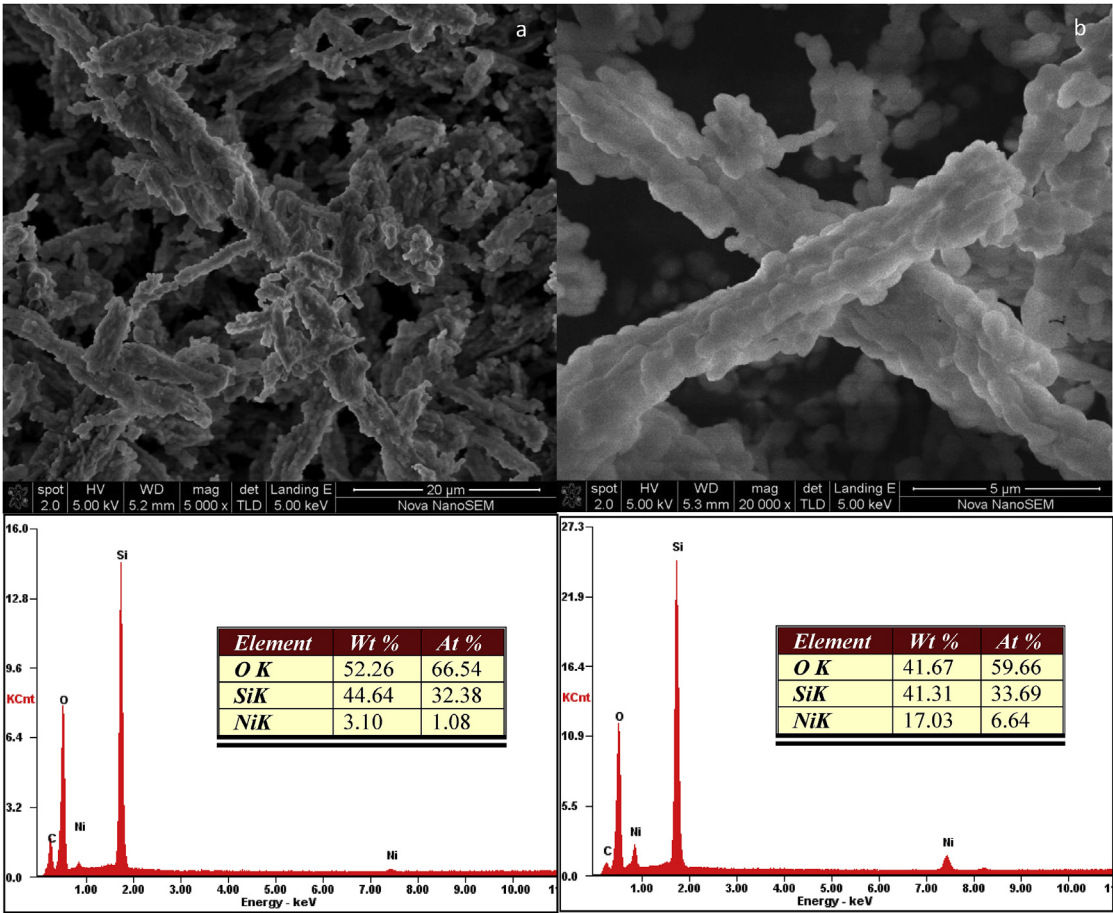

Fig. 7. SEM micrographs of the SBA-15 materials (upper): (a) Ni/SBA-15 (2.5) and (b) Ni/SBA-15 (10) with corresponding EDS analysis of different zones of the obtained micrographs (bottom).
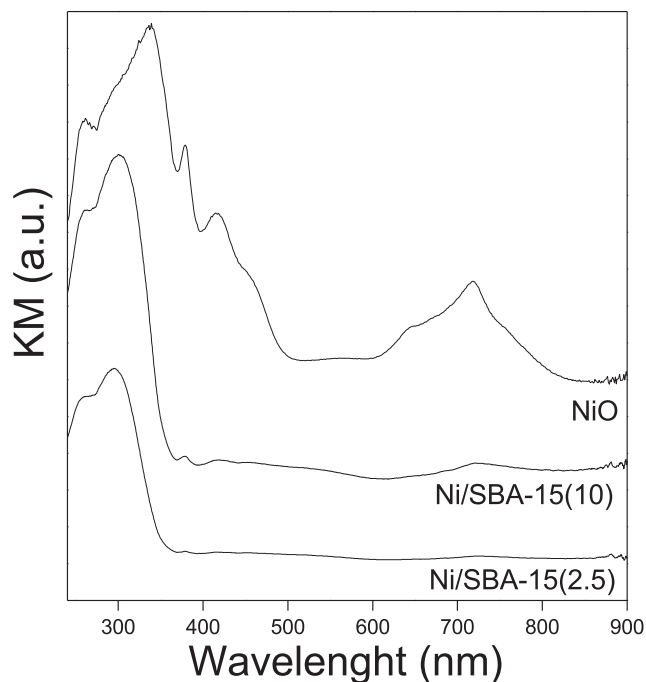
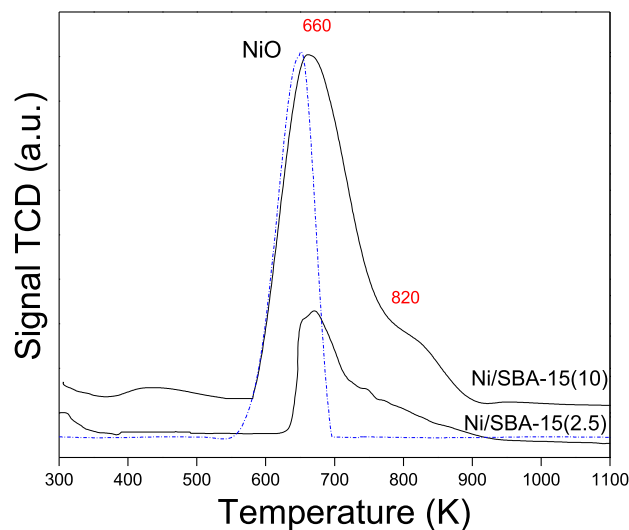Fig. 8. DRUV–vis spectra of NiO reference and the Ni/SBA-15 materials.

Fig. 10. TPR profiles of the Ni/SBA-15 materials and NiO.

suggested that the appropriate metal doping on the support (such as carbons, mesoporous silica) for hydrogen adsorption should be low [5,42].
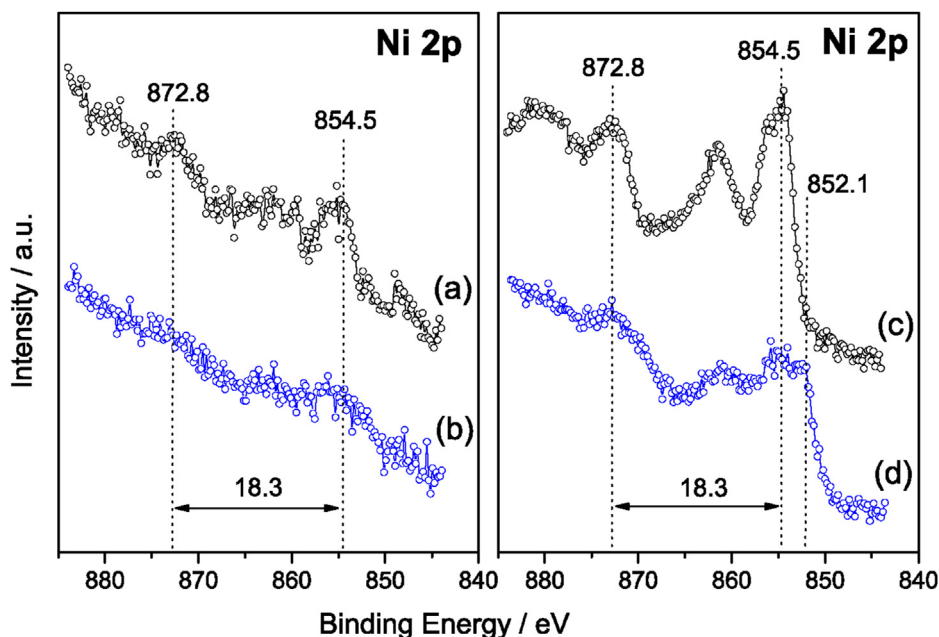

Fig. 9. XPS spectra for the materials: (a) Ni/SBA-15 (2.5), (b) Ni/SBA-15 (2.5)-R, (c) Ni/SBA-15 (10), (d) Ni/SBA-15 (10-R).

stronger interactions with hydrogen molecules due to the overlap of the potential fields from the opposing surfaces of the pore walls. According to this, Ni/SBA-15 (2.5) sample, that shows the highest hydrogen storage capacity, presents a slightly greater micropore volume.

In addition, the sample with the highest nickel loading (Ni/SBA-15 (10)) presents the lowest hydrogen storage capacity. This fact could be due to the increased number of NiO particles that cause a decrease in the S_{BET} and the pore volume, by obstructing the access of hydrogen towards some mesopore channels. Previous studies

Fig. 11 an also shows that the reductive treatment diminishes the hydrogen adsorption of the corresponding non-reduced samples. In our previous study [14], when the support used was MCM-41, the reductive treatment did not affect the H_2 adsorption at 77 K of the samples. This fact suggests that the nickel species involved in the H_2 adsorption at 77 K, are perhaps not reducible at those conditions due to highly dispersed and stabilized by the high interaction between them and the support. Therefore, here, the properties of the support employed (bigger mesopore channels and inter-connectivity) are related with the changes of the materials after the
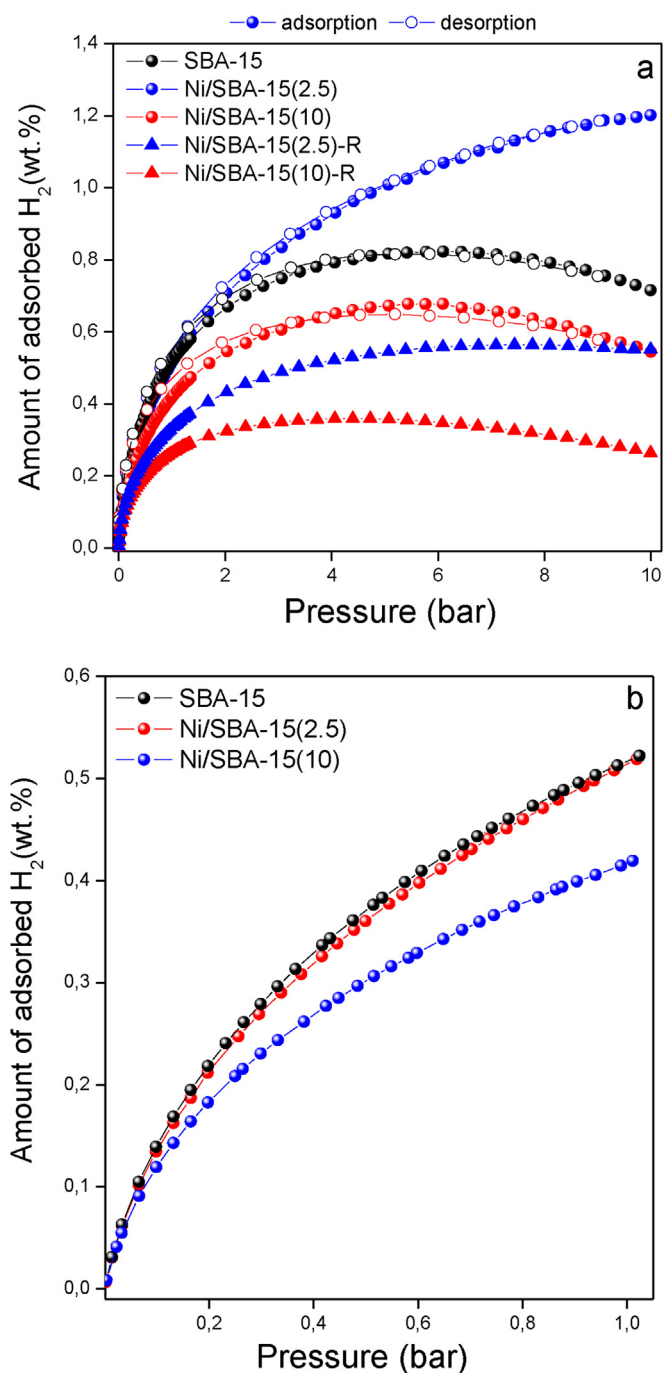
Fig. 11. H$_2$ adsorption-desorption isotherms of the unreduced and reduced Ni/SBA-15 materials at 77 K and high pressures (a) and low pressures (b).

reductive treatment, which have a negative effect in H$_2$ adsorption at 77 K. For example, the formation of larger Ni particles could diminish the number of low coordinated Ni sites. As a consequence, the nickel species involved in H$_2$ adsorption at 77 K are agglomerated into larger particles due to the reduction process. Thus, Richardson et al. [43] reported that the degree of reduction of NiO particles strongly depends on the particle size and morphology; due to two factors: diffusion limitation due to the particle size and differences in the microstructure of the particles caused by the same reduction process [44]. Richardson demonstrated that NiO crystallites of about 3 nm in size were transformed into Ni

crystallites of more than 20 nm, implying that Ni^0 ion transport following reduction was fast due to the close proximity of the NiO crystallites being reduced.

Hydrogen adsorption isotherms at 293 K up to 40 bar are shown in Fig. 12. At these experimental conditions, the following order in H$_2$ uptake was observed: Ni/SBA-15 (2.5) > Ni/SBA-15 (2.5)-R > SBA-15 > Ni/SBA-15 (10) ≈ Ni/SBA-15 (10)-R. Ni/SBA-15 (2.5) sample presented the highest H$_2$ adsorption, with an adsorbed hydrogen volume of 21.5 cm^3/g, corresponding to an overall uptake of 0.2 wt.%. From these results, it is clear that the reduction treatment does not improve hydrogen adsorption at these conditions. This fact is not in accordance with our previous reports [14], with the Ni/MCM-41 system, where the reduced samples stored higher amounts of H$_2$ than the unreduced ones. The results reported for the Ni/MCM-41 system were attributed to the small nickel particle size obtained by the incorporation of this metal inside the mesopores of MCM-41 (2 nm diameter). The results obtained in the Ni/SBA-15 system, can be explained by the larger metallic particle sizes obtained inside this material, due to its higher pore diameter (~8 nm), but also to its interconnectivity. As it can be observed, TEM images show larger dark areas over the channels, which correspond to NiO nanoparticle or Ni^0 agglomerates on the external surface. Thereby, the interconnectivity of the mesopores and the channel dimensions of the silica support would favor the agglomeration of nickel nanoparticles during the reductive treatment of supported NiO [45]. At the same time, the weak interaction with the support favors nickel particles agglomeration with the increased temperature.

In our previous report [14], we suggested the formation of a β-hydride phase in highly dispersed and reduced Ni nanoparticles on the MCM-41 support. This mechanism of hydride formation is dependent on the particle size of Ni^0 nanoparticles, because the particle size affects both the kinetics and the enthalpy of the hydride formation [46,47]. Some reports indicate that in all metal hydrides the kinetics of absorption-desorption can be improved by reducing the grain size of the metal. This fact allowed us to assert that the Ni particle size generated on the MCM-41 support would be the responsible for the eventual hydride formation. In the case of the Ni/SBA-15 samples, this mechanism would not be possible due to the larger Ni^0 particle size.

The trend observed in the non-reduced samples, shows that Ni/SBA-15 (2.5) presents the highest hydrogen adsorption. This is,
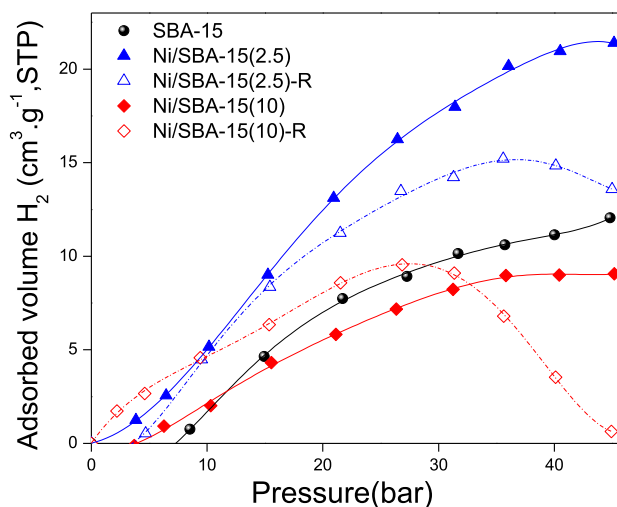

Fig. 12. H$_2$ adsorption-desorption isotherms at 293 K up to 40 bar of the unreduced and reduced Ni/SBA-15 materials.

again, different to the behavior observed with the Ni/MCM-41 materials. Despite that Ni/SBA-15 (2.5) has a S_{BET} smaller than the original SBA-15 by a ~18%, this sample shows a higher micropore volume, maybe created by the nickel oxide particles inside the pores. This kind of pores (with pore sizes minor than 2 nm) could be important in H_2 adsorption at room temperature, because of their highest adsorption potential, and would explain the trend of H_2 adsorption observed for SBA-15 and Ni/SBA-15 (2.5). On the other hand, when the nickel loading is higher, as is the case of Ni/SBA-15 (10) sample, nickel oxide or metallic nickel particles, block some porosity, diminishing both the S_{BET} and micropore volume of the samples, and diminishing H_2 adsorption at room temperature as well.

5. Conclusions

The influence of different factors (support, metal content, method of preparation) on the hydrogen storage capacity of Ni/SBA-15 materials prepared by wet impregnation method was investigated. A Ni/SBA-15 with low loading (2.1 wt.%) was the material with the maximum hydrogen adsorption capacity at 77 K, probably due to the presence of highly dispersed nickel species on the structure. In addition, it was observed that for Ni/SBA-15 supported materials, the reductive treatment has a negative effect in H_2 adsorption at 77 K, compared with non-reduced samples. This behavior was correlated with the textural properties of the SBA-15 (the size of the mesopore channels and its pore interconnectivity), that affect the properties and behavior of the supported nickel nanoparticles subjected to heat treatment.

On the other hand, the reduction treatment also does not improve hydrogen adsorption on Ni/SBA-15 at 293 K and 40 bar. This fact, again, is assigned to the particle size of the supported nickel nanoparticles that are located inside the mesoporosity of SBA-15, and which are highly affected by the porous characteristics of this material. These results are different to the behavior observed for the Ni/MCM-41 materials, and show the high dependence of pore size and its connectivity in Ni/SiO$_2$ materials for hydrogen storage applications.

Acknowledgements

References

[1] A. Zuttel, Naturwissenschaften 91 (2004) 157–172.
[2] Office of Energy Efficiency & Renewable Energy: https://energy.gov/eere/fuelcells/hydrogen-storage.
[3] M. Bastos-Neto, C. Patzschke, M. Lange, J. Mollmer, A. Moller, S. Fichtner, C. Schrage, D. Lassig, J. Lincke, R. Staudt, H. Krautscheid, R. Glaser, Energy Environ. Sci. 5 (2012) 8294–8303.
[4] S. Satyapal, J. Petrovic, C. Read, G. Thomas, G. Ordaz, Catal. Today 120 (2007) 246–256.
[5] M. Zielinski, R. Wojcieszak, S. Monteverdi, M. Mercy, M.M. Bettahar, Int. J. Hydrogen Energy 32 (2007) 1024–1032.
[6] E. Dundar-Tekkaya, Y. Yurum, Int. J. Hydrogen Energy 40 (24) (2015) 7636–7643.
[7] L. Wang, R.T. Yang, Catal. Rev. Sci. Eng. 52 (4) (2010) 411–461.
[8] N. Bouazizi, R. Ouargli, S. Nousir, R. Ben Slama, A. Azzouz, J. Phys. Chem. Solids 77 (2015) 172–177.
[9] S.H. Lee, T. Park, W. Yi, J. Kim, J. Nanosci. Nanotechnol. 15 (2015) 8922–8925.
[10] Y. Han, H. Kim, J. Park, S.H. Lee, J.Y. Kim, Int. J. Hydrogen Energy 37 (2012) 14240–14247.
[11] A.I. Acatrinei, M.A. Hartl, J. Eckert, E.H.L. Falcao, G. Chertkov, L.L. Daemen, J. Phys. Chem. C 113 (2009) 15634–15638.
[12] K.P. Prasanth, M.C. Raj, H.C. Bajaj, T.H. Kim, R.V. Jasra, Int. J. Hydrogen Energy 35 (2010) 2351–2360.
[13] P.M. Carraro, V.R. Elías, A.A. García Blanco, K. Sapag, S. Moreno, M.I. Oliva, G.A. Eimer, Microporous Mesoporous Mater. 191 (2014) 103–111.
[14] P.M. Carraro, A.A. García Blanco, F.A. Soria, G. Lener, K. Sapag, G.A. Eimer, M.I. Oliva, Microporous Mesoporous Mater. 231 (2016) 31–39.
[15] M. Jaroniec, M. Kruk, J.P. Olivier, Langmuir 15 (1999) 5410–5413.
[16] M. Kruk, M. Jaroniec, J. Phys. Chem. B 106 (2002) 4732–4739.
[17] K.S.W. Sing, Pure Appl. Chem. 57 (1985) 603–619.
[18] P.I. Ravikovitch, A.V. Neimark, Colloids Surfaces A Physicochem. Eng. Asp. 187–188 (2001) 11–21.
[19] P.I. Ravikovitch, A.V. Neimark, J. Phys. Chem. B 105 (2001) 6817–6823.
[20] R. Gómez-Reynoso, J. Ramírez, R. Nares, R. Luna, F. Murrieta, Catal. Today 107–108 (2005) 926–932.
[21] P. Van Der Voort, P.I. Ravikovitch, K.P. De Jong, A.V. Neimark, A.H. Janssen, M. Benjelloun, E. Van Bavel, P. Cool, B.M. Weckhuysen, E.F. Vansant, Chem. Comm. (2002) 1010–1011.
[22] V. Meynen, P. Cool, E.F. Vansant, Microporous Mesoporous Mater. 104 (2007) 26–38.
[23] L.A. Cano, A.A. García Blanco, G. Lener, S.G. Marchetti, K. Sapag, Catal. Today 282 (2017) 204–213.
[24] M. Tao, X. Meng, Y. Lv, Z. Bian, Z. Xin, Fuel 165 (2016) 289–297.
[25] M. Kruk, M. Jaroniec, Y. Sakamoto, O. Terasaki, R. Ryoo, C.H. Ko, J. Phys. Chem. B 104 (2000) 292–301.
[26] S. He, S. He, L. Zhang, X. Li, J. Wang, D. He, J. Lu, Y. Luo, Catal. Today 258 (2015) 162–168.
[27] D.J. Lensveld, J. Gerbrand Mesu, A. Jos van Dillen, K.P. de Jong, Microporous Mesoporous Mater. 44–45 (2001) 401–407.
[28] L. Wang, G. Li, W. Li, C. Ban, Y. Li, C. Guo, M. Zhang, L. Liu, N. Lu, M. Zheng, Chin. Chem. Lett. 25 (2014) 1620–1624.
[29] J. Liu, Y. Liu, W. Yang, H. Guo, H. Zhang, Z. Tang, F. Fang, Mater. Lett. 128 (2014) 15–18.
[30] T. Tsoncheva, L. Ivanova, J. Rosenholm, M. Linden, Appl. Catal. B Environ. 89 (2009) 365–374.
[31] D.G. Castner, P.R. Watson, I.Y. Chan, J. Phys. Chem. 93 (1989) 3188–3194.
[32] Y.M. Liu, Y. Cao, N. Yi, W.L. Feng, W.L. Dai, S.R. Yan, H.Y. He, K.N. Fan, J. Catal. 224 (2004) 417–428.
[33] S. Shen, F.P.S. Chen, Chow, P. Phanapavudhikul, K. Zhu, R.B.H. Tan, Micropor. Mesopor. Mater. 92 (2006) 300–308.
[34] A. Tirsoaga, D. Visinescu, B. Jurca, A. Ianculescu, O. Carp, J. Nanopart.. Res. 13 (2011) 6397–6408.
[35] V. Volkov, Z. Wang, B. Zou, J. Phys. Chem. Lett. 337 (2001) 117–124.
[36] K. Hadjiivanov, M. Mihaylov, D. Klissurski, P. Stefanov, N. Abadjieva, E. Vassileva, L. Mintchev, J. Catal. 185 (1999) 314–323.
[37] C.D. Wagner, W.M. Riggs, L.E. Davis, J.F. Moulder, G.E. Muilenberg, Handbook of X-ray Photoelectron Spectroscopy, Perkin-Elmer Corporation, Eden Prairie, 1979.
[38] L. Zhang, J. Li, Y. Cheni, J. Chem. Soc. Faraday Trans. 88 (14) (1992) 2075–20178.
[39] M. Tao, X. Meng, Y. Lv, Z. Bian, Z. Xin, Fuel 165 (2016) 289–297.
[40] A. Ungureanu, B. Dragoi, A. Chiriac, C. Ciotonea, D. Duprez, A.S. Mamede, E. Dumitriu, ACS Appl. Mater. Interfaces 5 (2013) 3010–3025.
[41] S. He, S. He, L. Zhang, X. Li, J. Wang, D. He, J. Lu, Y. Luo, Catal. Today 258 (2015) 162–168.
[42] D. Saha, S. Deng, Langmuir 25 (2009) 12550–12560.
[43] J.T. Richardson, R. Scates, M.V. Twigg, Appl. Catal. A Gen. 246 (2003) 137–150.
[44] D. Potoczna-Petru, L. Kepinski, Catal. Lett. 73 (2001) 41–46.
[45] T. Tsoncheva, L. Ivanova, J. Rosenholm, M. Linden, Appl. Catal. B Environ. 89 (3–4) (2009) 365–374.
[46] V. Berube, G. Chen, M.S. Dresselhaus, Int. J. Hydrogen Energy 33 (2008) 4122–4131.
[47] L. Zaluski, A. Zaluska, J. Ström-Olsen, J. Alloys Compd. 253–254 (1997) 70–79.